Au/CeO₂ Photocatalyst for the Selective Oxidation of Aromatic Alcohols in Water under UV, Visible and Solar Irradiation

Elisa I. García-López [1],*, Zahra Abbasi [2], Francesco Parrino [3], Valeria La Parola [4], Leonarda F. Liotta [4] and Giuseppe Marcì [5]

1. Department of Biological, Chemical and Pharmaceutical Sciences and Technologies (STEBICEF), University of Palermo, Viale delle Scienze, 90128 Palermo, Italy
2. Department of Chemistry, Faculty of Science, Shahid Chamran University of Ahvaz, Ahvaz 6135783151, Iran; zahra.abbasi886@gmail.com
3. Department of Industrial Engineering, University of Trento, Via Sommarive 9, 38123 Trento, Italy; francesco.parrino@unitn.it
4. Istituto per Lo Studio dei Materiali Nanostrutturati (ISMN)-CNR, Via Ugo La Malfa 153, 90146 Palermo, Italy; valeria.laparola@cnr.it (V.L.P.); leonardafrancesca.liotta@cnr.it (L.F.L.)
5. "Schiavello-Grillone" Photocatalysis Group, Department of Engineering, University of Palermo, Viale delle Scienze, 90128 Palermo, Italy; giuseppe.marci@unipa.it
* Correspondence: elisaisabel.garcialopez@unipa.it

Abstract: Au nanoparticles supported on CeO_2 have been prepared and investigated as photocatalysts for the photocatalytic selective oxidation of benzyl alcohol and 4-methoxybenzyl alcohol to the correspondent benzaldehydes, in aqueous suspensions and room conditions under UV, visible and natural solar light irradiation. Au nanoparticles have been supported by impregnation (1 and 3 wt.%) on two types of CeO_2 (i.e., a commercial one and a home prepared oxide obtained in the presence of NaOH as precipitation agent). The Au impregnated samples showed strong visible radiation absorption at 565–570 nm associated to localized surface plasmon resonance (LSPR). The bare CeO_2 samples are activated by UV light and resulted virtually inactive under visible irradiation, whereas the presence of Au improved both the conversion of the alcohols and the selectivity of the reaction towards the aldehyde, giving rise to good results, particularly under visible and natural solar light irradiation. The activity of the materials increased by increasing the Au content.

Keywords: plasmonic effect; CeO_2; Au-CeO_2; visible light photocatalysis

1. Introduction

The development of green and sustainable technologies is a big challenge of the current scientific research in applied sciences. The use of solar energy as clean and renewable energy source is a priority for the technologies aiming to develop photocatalytic transformations where the energy of photons can be used to drive many useful chemical reactions, including solar production of fuels, water purification and selective reactions.

In a photocatalytic process when a semiconductor is irradiated by suitable radiation, electrons are promoted from the valence band to the conduction band. The generation of electron/hole couples is responsible of oxidation and reduction processes. The photogenerated electrons reduce the adsorbed oxygen (O_2), if the process is carried out in air, to form superoxide radicals ($O_2^{-\bullet}$) and the photogenerated holes react with H_2O to form hydroxyl radicals ($OH^\bullet$), generally responsible for the oxidation of substrates resulting in their mineralization and/or partial oxidation [1].

The partial oxidation of alcohols to obtain aldehydes and/or ketones is one of the most important reactions in organic synthesis both, at industrial scale and in the laboratory. Photocatalysis is a promising technology for selective oxidation, alternative to traditional chemical methods based on reactions that are usually carried out at high temperatures and pressure with hazardous and harmful reagents. Photocatalytic reactions are carried out

under mild conditions (i.e., room temperature and atmospheric pressure with molecular oxygen or air as oxidant). The use of water for these reactions is highly desirable even if the selectivity can be lower with respect to the use of organic solvents. Photocatalysts responsive to visible light are particularly interesting, mostly those active under natural sunlight as the energy source.

The efficiency of the photocatalytic surface will depend on the light absorption ability that governs the number of active electrons/holes photoproduced. The greatest used photocatalysts are transition metal oxides, being TiO_2 the most popular. They require ultraviolet (UV) irradiation to induce photocatalytic reactions due to their relatively large band gap (ca. 3.2 eV for TiO_2). The total solar energy accounts only for ca. 5% of UV irradiation so they can be used with a moderate success also under sunlight. Consequently, the development of photocatalysts prone to be activated under visible light irradiation is paramountcy important from the practical point of view because visible light accounts for ~50% of the total solar energy. In this regard, metal nanoparticles such as gold (Au), silver (Ag) or copper (Cu) have been extensively studied as co-catalysts due to their unique properties associated with their strong photoabsorption in the visible light region, which is due to localized surface plasmon resonance (LSPR) [2].

As one of the rare earth oxides, with a bandgap of ca. 3.2 eV, CeO_2 has attracted intense interest because it plays an important role in environmental and energy related applications. The selective photocatalytic oxidation of benzyl alcohols into the corresponding aldehydes has been poorly investigated with CeO_2-based photocatalysts. Li et al. report that under different irradiation conditions CeO_2 showed some partial oxidation of benzyl alcohol to benzaldehyde in water. The benzyl alcohol conversion achieved 27% in the presence of CeO_2 and 33% when Pt/CeO_2 was used; whereas the selectivity to benzaldehyde was 12% or 37% in the presence of CeO_2 or $Pt-CeO_2$, respectively, after 5 h of reaction under irradiation with a 300 W Xe lamp [3].

Recently, a great deal of research has been conducted in order to understand the catalytic activity of CeO_2-supported noble metals such as Au, Pt and Ag. An enhanced photodegradation of organic compounds has been largely reported after adding Au or Ag nanoparticles to the surface of semiconductor photocatalysts, including CeO_2 [4]. These metal nanoparticles (MNPs) have been used in photocatalysis for the inhibition of the recombination of the photogenerated electron/hole couples because they are excellent scavengers of electrons [5]. An alternative benefit of using metal NPs is their localized surface plasmon resonance (LSPR, commonly called as SPR), which results from the confinement of a surface plasmon in a nanoparticle (NP) smaller than the wavelength of light exciting the plasmon (i.e., when a NP is irradiated, the oscillating electric field causes the coherent oscillation of conduction electrons) [2]. Irradiating metal nanoparticles with light at their plasmon frequency generates intense electric fields at the surface of the nanoparticles. The frequency of this resonance can be tuned by varying the nanoparticle size, shape, material, and proximity to other nanoparticles [6].

The use of a semiconductor supporting metal NPs gives rise to a plasmonic photocatalysts where the mechanism of the electron/hole photogeneration is improved by the visible activated plasmon resonance [7]. Absorption of light is a characteristic property of metal NPs, particularly for Au, Ag and Cu NPs which are visible to the unaided eye, indeed, the peaks of photoabsorption due to SPR of Au, Ag and Cu nanoparticles are generally observed at around 550, 450 and 600 nm, respectively. In contrast to reports on supported Au nanoparticles, less research has been published on chemical reactions induced by the SPR of Ag and Cu nanoparticles, probably due to their instability under working conditions.

The plasmonic effect of metal NPs has found applications in medical therapy, surface-enhanced Raman spectroscopy, etc. [8]. Kozuka et al. carried out pioneer work introducing Au and Ag on the TiO_2 layer in photoelectrochemical (PEC) evaluation [9]. Great advances have been achieved in this field, and plasmonic photocatalysts have become a promising strategy for developing efficient visible-light-responsive composite materials.

The photocatalytic activity of these nanocomposites was enhanced due to the following two physical effects: (i) The SPR-induced light for enhancing the light absorption and (ii) the electron transfer from the metal to the oxide in the Au/semiconductor structure [10–12]. Many reports have been devoted to the use of Au/CeO$_2$ photocatalysts for dye bleaching but more interestingly, recent literature explores their application as robust photothermal catalysts active under solar irradiation for CO$_2$ reduction [13]. The selective oxidation of alcohols to their corresponding aldehydes in water, the greenest solvent for photocatalytic reactions, is an important organic transformation, because aldehydes are widely used in food, pharmaceutical and chemical industries [14].

Li et al. studied Au/CeO$_2$ hybrid nanofibers as photocatalysts for selective oxidation of benzyl alcohol to benzaldehyde in acetonitrile using a Xe lamp and a filter to get just visible irradiation ($\lambda > 420$ nm). They obtained a complete conversion of BA to BAL by using increasing loading amounts of Au NPs from 0.25 to 2.5 wt.% showing SPR absorption centered at ca. 605 nm [15]. The reaction rate obtained was in the range 500 to 2250 µmol h^{-1} g^{-1} by using the Xe lamp and from 50 to 400 µmol h^{-1} g^{-1} when the system was irradiated with $\lambda > 420$ nm. Kominami et al. prepared Au/CeO$_2$ nanocomposites exhibiting SPR absorption at ca. 550 nm, so they used a green LED as irradiation source [16]. The intensity of the photoabsorption due to the SPR of Au was higher for Au NPs with bigger size. The photocatalytic oxidation of benzyl alcohol in aqueous suspensions of Au/CeO$_2$ samples gave rise to a 100% conversion of the substrate to benzaldehyde in ca. 15–20 h. The rates of benzaldehyde formation were in the range 1.9 to 3.0 µmol h^{-1}.

According to the literature, the most important factors influencing the activity and selectivity of Au/CeO$_2$ as thermal catalysts for the partial oxidation of benzyl alcohols are the size of the supported gold nanoparticles [17] and the concentration of lattice defects in the ceria support [18]. Wolsky et al. report that the use of NaOH as precipitation (or coprecipitation) agent instead of urea or hexamethylenetetramine in the CeO$_2$ preparation has a significant impact on the structure, texture and catalytic properties of Au/CeO$_2$ catalysts resulting beneficial in the formation of small and uniform gold nanoparticles possessing enhanced catalytic activity s in low-temperature oxidation of benzyl alcohol [19].

Based on the so far reported literature, we have considered it of interest to investigate the properties and photocatalytic activity of two sets of Au catalysts, with loading 1 and 3 wt.%, deposited on ceria. One set of samples is based on commercial CeO$_2$, and the other one is based on a home prepared (hp) CeO$_2$ oxide using NaOH, as precipitating agent. The prepared samples were used as photocatalysts for the selective oxidation of both benzyl alcohol and 4-methoxy benzyl alcohol to the corresponding aldehydes in water and aerobic environment under UV, visible and solar irradiations. In particular, this study investigates for the first time how two types of ceria (one commercial and one home prepared) both pure and loaded with gold are able to exploit either UV or Vis radiation for partial photocatalytic oxidation reactions of alcohol. In fact, UV radiation is able to make ceria work as a photocatalyst and visible radiation to promote the plasmonic effect on Au nanoparticles. Furthermore, by making the reactions take place using natural solar radiation, the possible synergistic effect between the two effects (photocatalytic and plasmonic) was studied.

2. Results and Discussion

2.1. Characterisation of the Au/CeO$_2$ Photocatalysts

The XRD patterns of the Au catalysts supported on commercial and hp ceria are shown in Figure 1A,B, respectively. In all cases, the diffraction peaks of the fluorite structure of ceria were detected, with a more crystalline structure in the case of the Aldrich sample. In Table 1 the support crystallite sizes and the gold particle sizes, as determined from the line broadening of the CeO$_2$ and metal Au (111) XRD peaks, are listed. No gold signals are visible in the XRD patterns of both Au1% catalysts, while slightly detectable features were observed in the case of the Au3% catalysts, corresponding to an average size of ca. 3.5 and ca. 2.5 nm, in the case of the CeO$_2$ Aldrich and the hp supported samples, respectively.
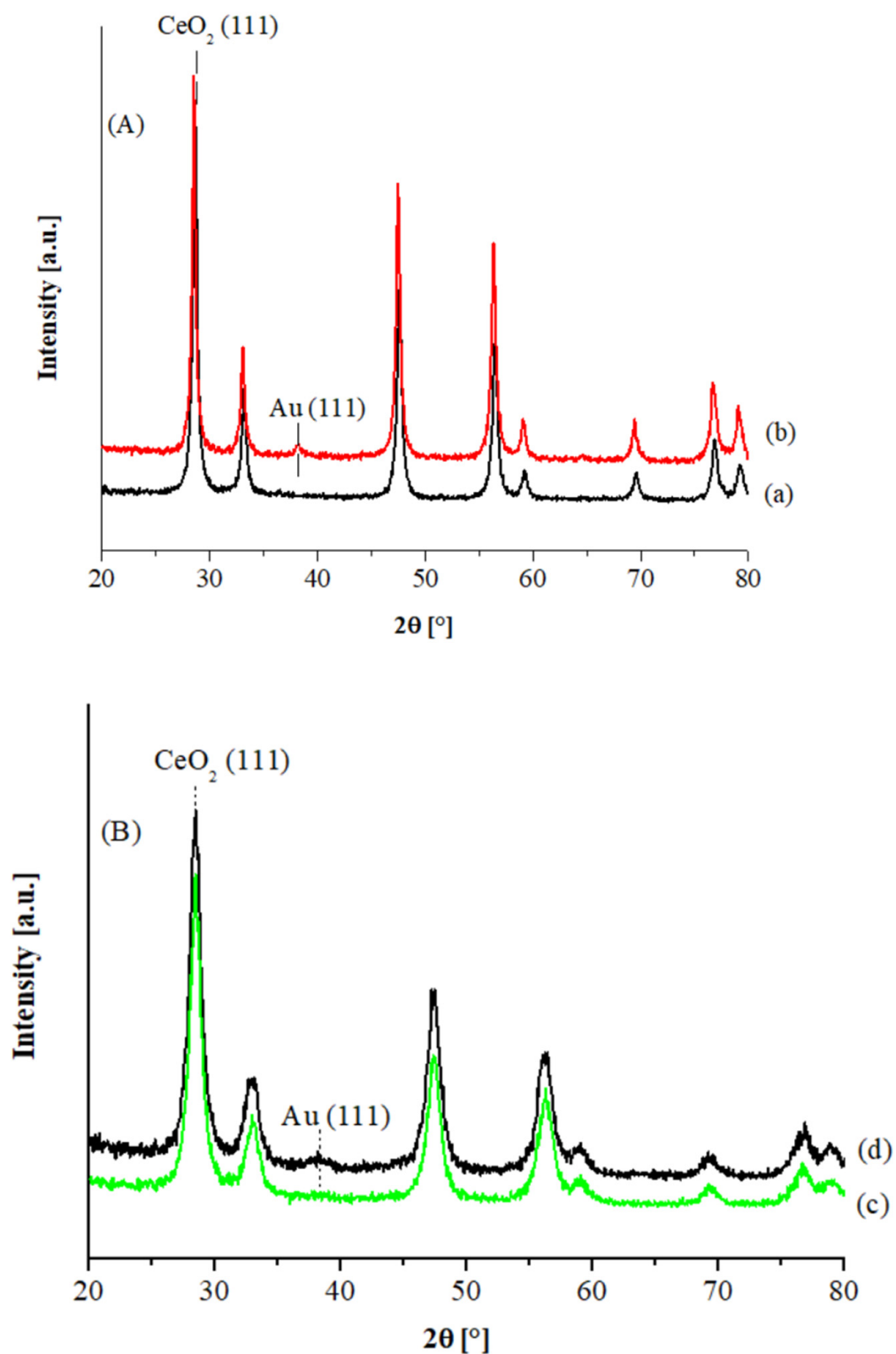
Figure 1. XRD patterns of: (**A**) Au/CeO$_2$ Aldrich: (a) 1%Au/CeO$_2$ A, (b) 3%Au/CeO$_2$ A; (**B**) Au/CeO$_2$ home prepared: (c) 1%Au/CeO$_2$ hp; (d) 3%Au/CeO$_2$ hp.

**Table 1.** Textural properties of ceria oxides and Au supported catalysts.

Sample	SSA [m² g⁻¹]	Mean Mesopore Diameter (BJH) nm	Mesopore Volume [cm³ g⁻¹] [1]	Micropore Volume [cm³ g⁻¹] [2]	Crystallite Size [nm] [3]
CeO₂ A	79.0	12.3	0.22	-	22.0
1%Au/CeO₂ A	77.0	11.7	0.20	-	18.0 (nd)
3%Au/CeO₂ A	75.0	10.8	0.19	-	18.0 (3.5)
CeO₂ hp	101.0	6.0	0.69	0.0090	10.0
1%Au/CeO₂ hp	99.0	6.0	0.68	0.0086	12.0 (nd)
3%Au/CeO₂ hp	95.0	6.0	0.64	0.0077	12.0 (2.5)

[1] By BJH method; [2] By t-Plot; [3] CeO_2 crystallite size and Au particle size (in parenthesis) determined by Debye-Scherrer equation.

In Figure 2A,B the nitrogen adsorption–desorption isotherms and pore size distribution curves are displayed for CeO_2 A, CeO_2 hp and for the corresponding Au catalysts. The isotherms are classical type IV, as defined by IUPAC, with hysteresis typical of mesoporous materials, H1-H2 types. The adsorption–desorption curves, for CeO_2 hp and the corresponding Au catalysts, result at low p/p_0 values in a relatively larger adsorption than for CeO_2 A and the related catalysts, suggesting that the former samples contain also some micropores (see Table 1).

In Table 1 the specific surface area (SSA), mesopore diameter and mesopores volume values are listed. The micropore volume calculated by t-Plot for CeO_2 hp and the corresponding gold supported catalysts is also reported. Both ceria oxides are characterized by relatively high SSA, ~80 and 100 m²/g, respectively. After Au deposition and calcination, for both catalysts the surface area values along with the pore volume slightly decreased. For the Au catalysts over CeO_2 A the mean pore diameter also decreased, suggesting that some metallic Au nanoparticles may partially fill the pores, while no modifications were observed in the pore size distribution of gold deposited over CeO_2 hp, according to the stabilization of gold mainly as Au^{+1} species that partially diffuse into the bulk of the support. Furthermore, the Au/CeO_2 hp catalysts kept some microporosity based on the micropore volume values listed in Table 1.

The SEM micrographs shown in Figures 3 and 4 are useful to study the morphology of the investigated samples. Figure 3 reports the micrographs of the samples based on the home prepared CeO_2 material. The CeO_2 hp sample (prepared in the presence of NaOH) consists of aggregates of nanoparticles whose size ranged between ca. 24 and ca. 40 nm. The empty spaces between these particles have roughly the same size of the particles and thus this sample appears to be essentially mesoporous. As far as the commercial CeO_2 A (Aldrich) is concerned, as shown in Figure 4, it is constituted of aggregates of nanoparticles as well, even if in this case their size is generally smaller (14–25 nm) than those of the CeO_2 hp sample. However, the biggest differences between CeO_2 A and CeO_2 hp sample are observed in the nanoparticles aggregation manner. Indeed, in the CeO_2 A catalyst, in addition to the presence of mesopores, existing in the CeO_2 hp, are also observed macropores. The morphology of the CeO_2 A catalyst looks like that of certain volcanic rocks. For all Au catalysts, the presence of 1% or 3% Au does not modify significantly the morphology of the corresponding ceria supports, in agreement with the so far discussed SSA and porosity values (Table 1).
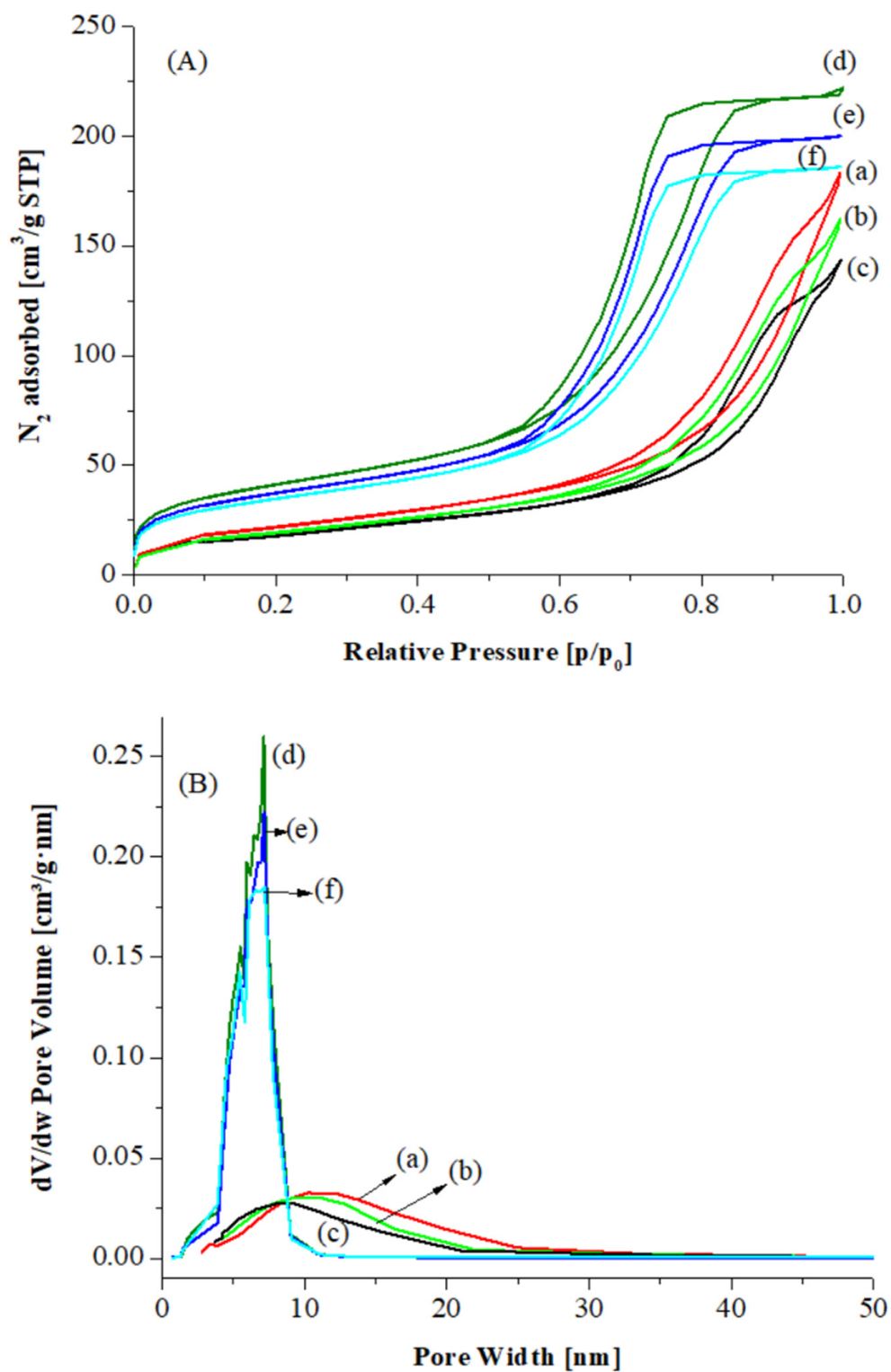
Figure 2. (**A**) Nitrogen adsorption–desorption isotherms and (**B**) pore size distribution curves for CeO_2 A and CeO_2 hp samples and for the corresponding Au catalysts: (a) CeO_2 A; (b) 1%Au/CeO_2 A, (c) 3%Au/CeO_2, (d) CeO_2 hp; (e) 1%Au/CeO_2 hp; (f) 3%Au/CeO_2 hp.
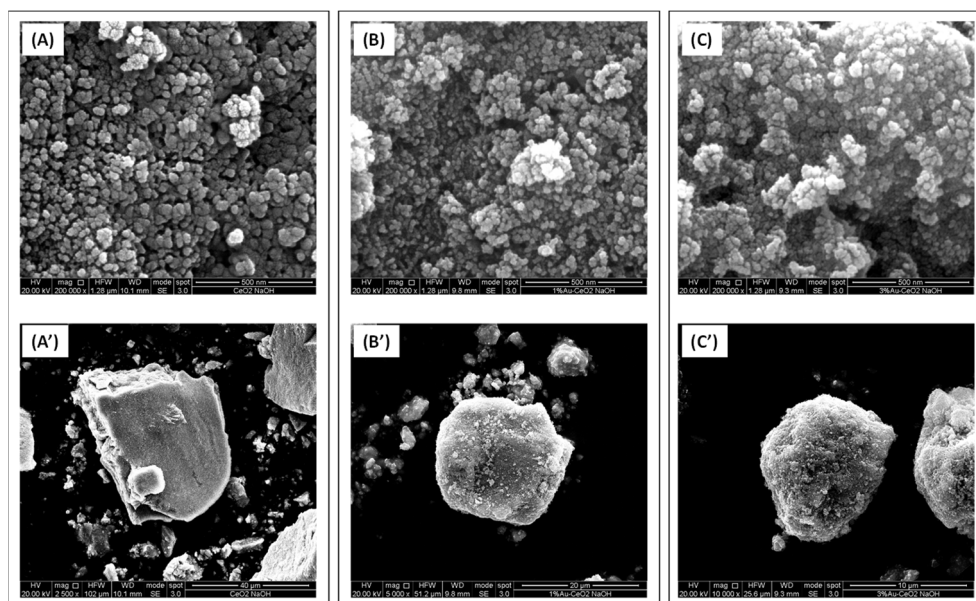
Figure 3. SEM micrographs of the prepared powders at two different magnifications for (**A**,**A′**) bare CeO_2 hp; (**B**,**B′**) 1%Au/CeO_2 hp and (**C**,**C′**) 3%Au/CeO_2 hp.
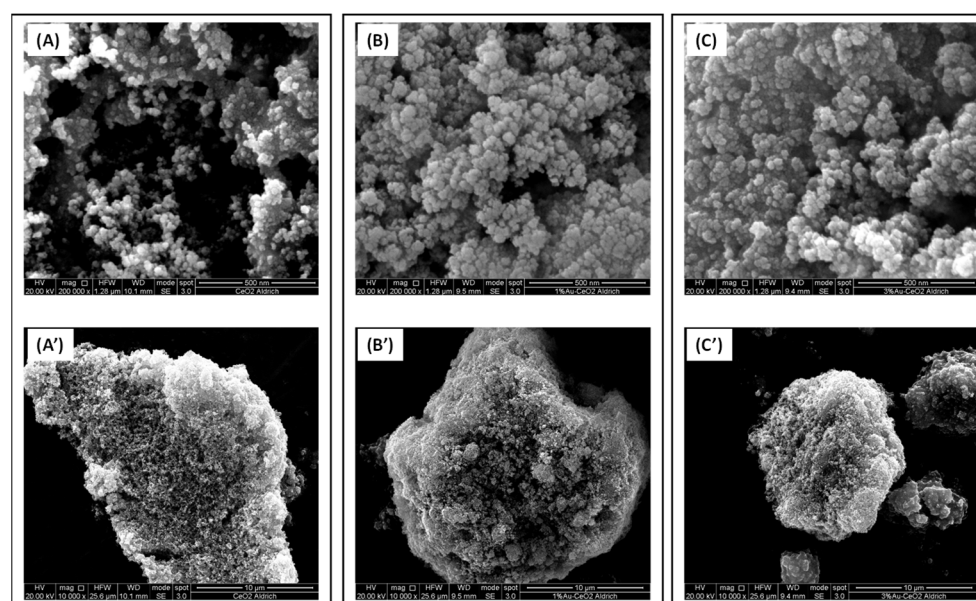
Figure 4. SEM micrographs of the prepared powders at two different magnifications for (**A**,**A′**) bare CeO_2 A; (**B**,**B′**) 1%Au/CeO_2 A and (**C**,**C′**) 3%Au/CeO_2 A.

As far as the Au content detected by EDX investigation is concerned, it can be noted that the two samples with a nominal content of 1% seem a little richer in the metal. Indeed, for the 1% Au-CeO_2 hp and 1% Au-CeO_2 A the Au content measured was 1.7% and 1.4%, respectively. On the contrary, in the case of the two catalysts with the higher Au content, the EDX result is practically coincident with the nominal one, 3.2 and 3.1 for the 3% Au-CeO_2 hp and 3% Au-CeO_2 A samples, respectively. The higher amount of gold detected by EDX for both 1% Au catalysts is in agreement with the higher metal dispersion with respect to the 3% Au samples.

Scanning/transmission electron microscopy was used to get information on the morphology of the samples. The cubic morphology of the bare CeO_2 Aldrich and hp is apparent in the micrographs (a) and (d), respectively, of Figure 5. While the Aldrich sample appears

more homogeneous, some elongated particles can be noted in the hp sample. The presence of gold has been highlighted through EDXS mapping as shown in micrographs (b2) and (e2) for the samples containing 1% gold, and through high-angle annular dark-field (HAADF) detector coupled with EDXS analysis of selected areas for the samples containing 3% gold. Gold is homogeneously distributed throughout the samples and it is present mainly as spherical nanoparticles ranging between 2 and 3 nanometers with some bigger aggregates up to 6 nanometers.
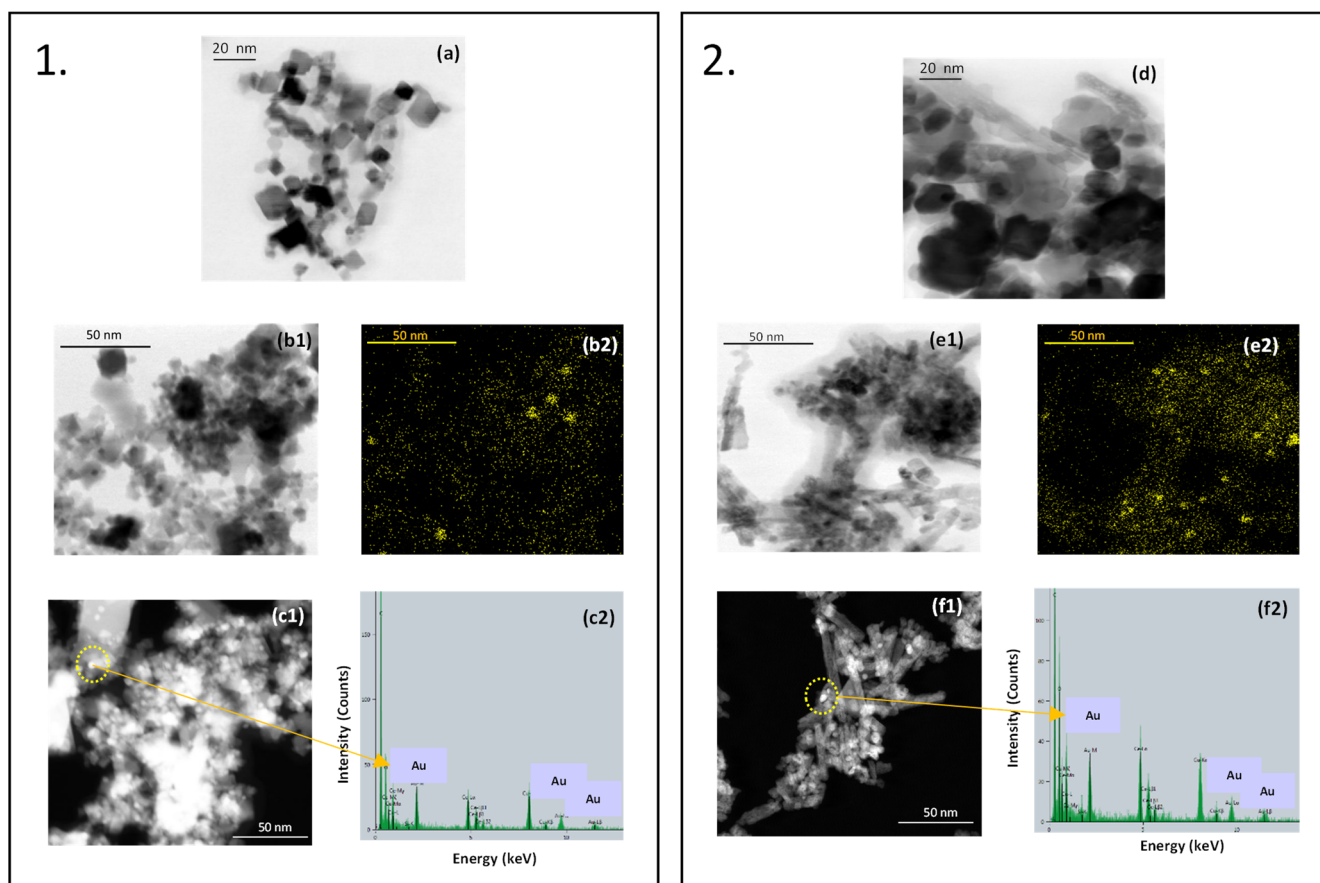
Figure 5. S/TEM-EDX analysis of Aldrich CeO_2 based samples (**Panel 1**) and hp CeO_2-based samples (**Panel 2**). Bare CeO_2 A sample (**a**); 1%Au/CeO_2 A micrograph with BF detector (**b1**) and corresponding EDXS map for Au distribution (**b2**); 3%Au/CeO_2 A micrograph with HAADF detector (**c1**) and corresponding EDXS spectrum of the yellow highlighted area (**c2**). Bare CeO_2 hp sample (**d**); 1%Au/CeO_2 hp micrograph with BF detector (**e1**) and corresponding EDXS map for Au distribution (**e2**); 3%Au/CeO_2 hp micrograph with HAADF detector (**f1**) and corresponding EDXS spectrum of the yellow highlighted area (**f2**).

To get deep insight into the chemical composition of the catalysts, the samples were further characterized using XPS. Cerium region is very complex and the determination of the relative percentage of Ce(III) and Ce(IV) is usually done according to the initial classification by Burrough [20] with ten components (six for the Ce3d5/2–Ce3d3/2 of Ce(IV) and four for Ce3d5/2–Ce3d3/2 of Ce(III)). Anyway, the correct evaluation of the relative percentage of the two different oxidation states, suffer of the complexity of the region. For comparison reasons, it is possible to use the simplification proposed by Henderson [21]. In agreement with this method, the Ce(IV)% is estimated by calculating the attenuation of the u''' component at 917 eV with respect to the total area of the Ce3d peak. According to their

study in a pure CeO$_2$ oxide the u′′′ component would be 14% of the total Ce3d area. The Ce(III) content in % is then calculated by using Equation (1):

$$Ce(III)\% = 100 - Ce(IV)\% = 100 - (100 * (u'''/14)) \tag{1}$$

where u′′′ is the area fraction of the peak at 917 eV [22,23].

Ce (III)–Ce(IV) relative amount was calculated applying this method (see Figure 6A). Moreover, in order to minimize cerium reduction by the beam, for all samples, Ce region was recorded with a fast modality (3 min each scan). The results obtained are compiled in Table 2. The samples supported on CeO$_2$ hp show a higher percentage of Ce(III) with respect to the samples prepared on CeO$_2$ A. Gold nature is sensitive to the support type. For CeO$_2$ A both samples show an Au 4f7/2 peak centered at 84.5 ± 0.3 eV typical of metallic gold, while the CeO$_2$ hp supported series exhibit for both composition the Au 4f7/2 peak centered at 85.4 ± 0.3 eV typical of Au^{+1} species [24]. These results coupled with the increase of Ce(III) in CeO$_2$ hp supports point out a withdraw of electron from gold to CeO$_2$ in the hp series. Moreover, for the samples CeO$_2$ hp the FWHM of gold peak is quite high indicating the presence of several slightly different chemical environments for gold. For both series, the increase of the amount of gold caused a decrease of cerium reduction probably due to the formation of bigger particles, as seen by XRD, which lessen the influence of gold on ceria.
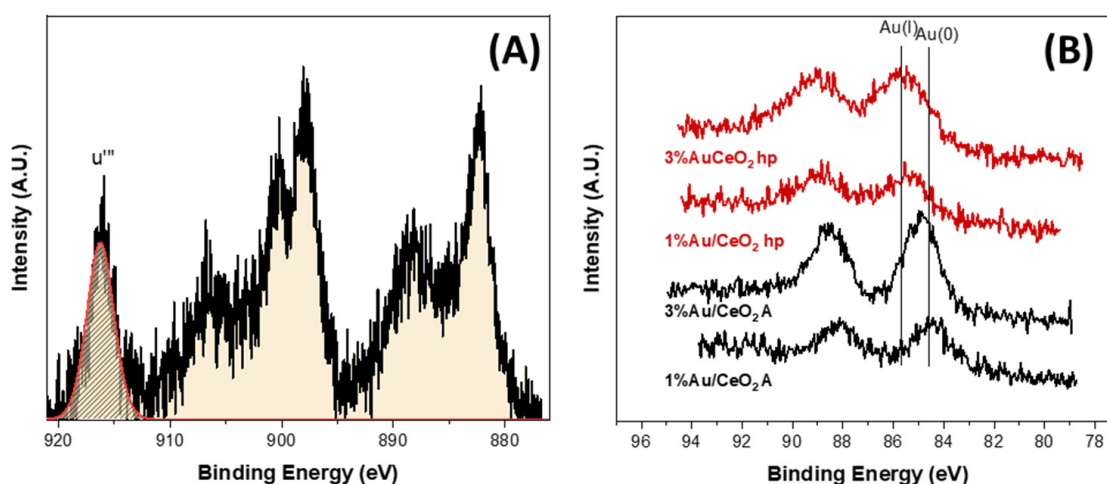

Figure 6. (**A**) Ce3d XP spectrum of 1%Au/CeO$_2$ A and (**B**) Au 4f XP spectra of all Au supported catalysts.

Table 2. XPS data of the two series of Au/Ceria catalysts in terms of Ce(III)/Ce(IV) percentages, Au 4f5/2 binding energy and Au/Ce atomic ratios. The values calculated by EDX and the nominal Au/Ce ratios are reported for comparison.

Sample	Ce(III) [%]	Ce(IV) [%]	Au 4f5/2 [eV] [a]	Au/Ce (XPS)	Au/Ce (EDX)	Au/Ce Nominal Value
1%Au/CeO$_2$ A	14	86	84.3 (1.7)	0.05	0.014	0.010
3%Au/CeO$_2$ A	13	87	84.8 (1.7)	0.18	0.032	0.030
1%Au/CeO$_2$ hp	18	82	85.2 (2.3)	0.06	0.017	0.010
3%Au/CeO$_2$ hp	15	85	85.6 (2.6)	0.11	0.033	0.030

[a] In parenthesis the FWHM of Au 4f5/2 component.

Table 2 reports the XPS-derived Au/Ce atomic ratio along with the above commented EDX atomic ratio. As expected by the surface nature of XPS technique, the XPS-derived ratio are higher than the EDX derived ratio by a factor of ca. 3 for all samples except than 3%Au/CeO$_2$ A where the Au/Ce by XPS is 5.6 higher than the one by EDX. This fact is

probably due to the smaller pore diameter of CeO$_2$ A. which causes a minor diffusion of gold precursors inside the pores with a more pronounced surface deposition emphasized by XPS analysis. On the other hand, it is likely that Au^{+1} species tend to diffuse into the bulk of CeO$_2$ hp oxides being less detectable on the surface.

Diffuse reflectance spectroscopy (DRS) has been employed to study the optical properties of the samples. Figure 7 shows the DRS of the CeO$_2$ and Au/CeO$_2$, along with their absorption of UV light. The DRS of the CeO$_2$ and Au/CeO$_2$ samples, depicted in Figure 7A evidenced that both CeO$_2$ showed only one absorption edge around 400 nm corresponding to the band gap energy of the semiconductor, whereas for the Au supported materials, the visible light absorbance was evident, as revealed in Figure 7B corresponding to the Kubelka-Munk function F(R$_\infty$) of the diffuse reflectance spectra, which can be assumed as the absorption of the samples. The plasmonic absorption band of the Au is observed at 575 and 560 nm for the Au/CeO$_2$ A and Au/CeO$_2$ hp samples, respectively. The SPR absorption becomes more intensive as the Au loading increases from 1% to 3 wt.%. The increased visible light absorption from Au SPR should help enhance the harvesting of solar energy and promote related photocatalytic processes.
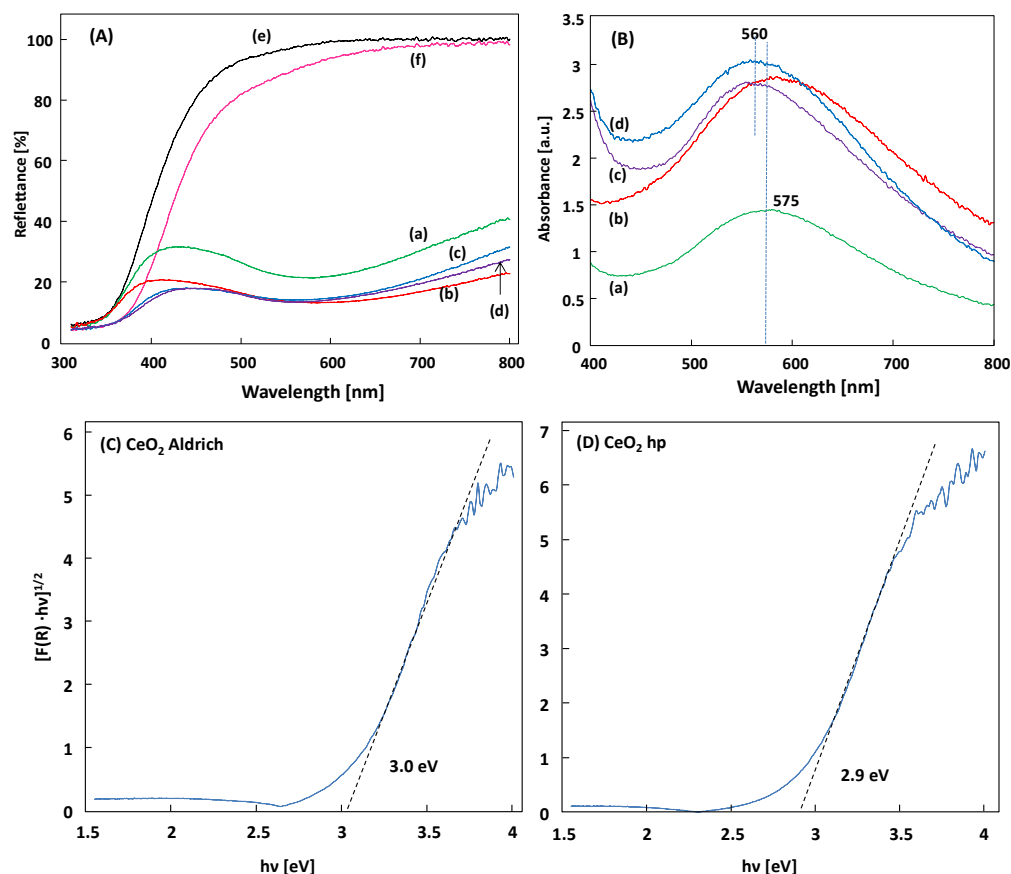
Figure 7. (**A**) DRS and (**B**) absorption spectra of the samples: (a) 1%Au/CeO$_2$ A; (b) 3%Au/CeO$_2$ A; (c) 1%Au/CeO$_2$ hp; (d) 3%Au/CeO$_2$ hp; (e) CeO$_2$ A; (f) CeO$_2$ hp and (**C,D**) Tauc plot of CeO$_2$ A and CeO$_2$ hp samples, respectively.

Ke et al. supported Au nanoparticles on different oxides, including CeO$_2$ and TiO$_2$, among others, to test these photocatalysts under visible light for the reduction of ketones to alcohols. They reported the DRS spectra of the powders and comparing Au/CeO$_2$ with Au/TiO$_2$, the LSPR band of Au/CeO$_2$ resulted red shifted and a more intense peak was recorded for the one of Au/TiO$_2$. They suggested a stronger LSPR effect of Au/CeO$_2$, explaining the stronger absorption light of Au/CeO$_2$ by a possible strong interface action between Au nanoparticles CeO$_2$ that those existing in the Au/TiO$_2$ powder [25]. The

red-shift of the LSPR band for the present samples, with respect to those observed by Ke (ca. 520 nm), could indicate a strong interaction with the CeO_2 support, particularly in the case of the CeO_2 A samples.

To determine the optical band gap energy of the materials, the Kubelka-Munk function $F(R_\infty)$ of the diffuse reflectance spectra has been used and the band gap value was estimated by extrapolating a linear fitting in the Tauc plot [26] (i.e., the plot of $(F(R_\infty) \cdot h\nu)^{1/2}$ vs. the incident light energy in eV) by considering the CeO_2 as an indirect semiconductor, as shown in Figure 7C,D. The presence of Au on the surface of CeO_2 does not change the E_{gap} nevertheless it affords absorbance in the visible region, so that both UV and visible radiation can contribute to the photoactivity of the powders [27]. In addition, the photoactivity can increase via the delay of the recombination rate of photogenerated electron and hole pairs [28].

2.2. Photocatalytic Activity under UV or under Visible Light Irradiation

All the Au/CeO_2 powders showed to be photoactive under UV and, as well, under Vis light irradiation for the photocatalytic partial oxidation of both alcohols. The results obtained for the selective oxidation of benzyl alcohol (BA) and 4-methoxy benzyl alcohol (4-MBA) in water, in terms of alcohol conversion and selectivity to the corresponding aldehyde after 4 h of reaction, are reported in Table 3.

Table 3. Conversion percentage (X) of BA and 4-MBA and selectivity percentage (S) towards the corresponding aldehyde after 4 h of UV or visible (VIS) irradiation.

Catalyst	BA				4-MBA			
	UV		VIS		UV		VIS	
	X	S	X	S	X	S	X	S
CeO_2 A	-	-	-	-	11	25	8	7
1%Au/CeO_2 A	2	100	5	100	20	72	22	98
3%Au/CeO_2 A	4	100	6	100	35	78	44	95
CeO_2 hp	-	-	-	-	5	18	-	-
1%Au/CeO_2 hp	2	100	4	100	6	19	7	40
3%Au/CeO_2 hp	2	100	5	100	13	75	15	100

The perusal of Table 3 shows that by irradiating the system containing a benzyl alcohol suspension with both UV or visible light, the CeO_2 pristine powders resulted completely inactive, whereas a modest conversion of BA was observed in the presence of Au-loaded CeO_2 samples showing a selectivity to benzaldehyde of 100%. As a general consideration, the conversion values were, for any photocatalyst, nearly the same by irradiating with UV light or under visible irradiation, albeit for the latter the presence of Au seemed to be slightly beneficial.

The conversion of 4-MBA was much higher than that obtained for BA and the selectivity to 4-MBAL was remarkable only in the case of the samples loaded with Au. Under UV irradiation, both CeO_2 pristine powders gave rise to a certain conversion, slightly higher for the commercial powder, as reported in Table 3. Interestingly, only the CeO_2 A sample gave rise also conversion of 4-MBA under visible light irradiation. The Au/CeO_2 samples lead to a higher conversion of the alcohol than the pristine CeO_2, and the conversion increased by increasing the Au amount. The Au supported samples resulted particularly active by using the CeO_2 A as support. These samples showed higher conversion of 4-MBA under visible irradiation than under UV light. The most active sample in terms of conversion resulted to be the 3%Au/CeO_2 A, particularly under visible light. Selectivity to 4-MBAL under UV irradiation resulted 25% and 18% for the pristine CeO_2 A and hp, respectively. The presence of Au on both of the supports increased not only the conversion but also the selectivity to the aldehyde and in general the activity increased by increasing the Au content. The most active sample in terms of conversion and selectivity resulted the 3%Au/CeO_2 A, followed by the 3%Au/CeO_2 hp. These insights evidence that the photocatalysts based on the CeO_2

hp are in general less oxidant than the analogous based on the commercial CeO_2 A. This behavior is the same than that observed for the BA partial oxidation, albeit BA resulted by far more difficult to be oxidized than 4-MBA. The Au-loaded CeO_2 materials can be used under visible light irradiation for 4-MBA partial oxidation quite successfully. Furthermore, these materials seem more effective under visible light irradiation with respect to UV light.

The mechanism of the photo-oxidation in the presence of Au nanoparticles is distinctly different from that of the semiconductor photocatalysts. Indeed, in a photocatalytic process when a semiconductor is irradiated by suitable radiation, electrons are promoted from the valence band to the conduction band. Consequently, the generated electron/hole couples are responsible of oxidation and reduction processes. The photogenerated electrons reduce the adsorbed oxygen (O_2), if the process is carried out in air, to form superoxide radicals ($O_2^{-\bullet}$) and the photogenerated holes react with H_2O to form hydroxyl radicals ($OH^{\bullet}$), generally responsible for the oxidation of substrates resulting in their mineralization and/or partial oxidation. On the contrary, irradiated Au-NPs are able to absorb visible light due to the surface plasmon resonance effect. This effect is due to the joint oscillation of conduction electrons in the gold NPs which, resonating with the electromagnetic field of the incident light, give rise to a significant enhancement of the local electromagnetic fields near the surfaces of the Au-NPs. Consequently, the conducting electrons on the NP surfaces increase their energy content and they can interact with the O_2 molecules adsorbed on the surface of Au-NP or even on the support surface to form superoxide radicals ($O_2^{-\bullet}$). Furthermore, the excited electrons may relax back to their equilibrium states and release heat to the Au-NP lattice, resulting in a rapid and localized heating of the Au-NPs [25]. Such two effects can induce together chemical reactions of adsorbed molecules both on the Au-NPs and on the support. Furthermore, the localized heating of the Au-NPs can favorite the desorption of the reaction intermediate. In the case of the reactions reported in this study, the desorption of the formed aldehydes is of paramountcy importance to avoid their successive oxidation to benzoic acids that are responsible for the blockage and consequently the inactivation of the catalytic sites [29].

To explain the higher conversion of 4-MBA with respect to BA by using the same photocatalyst and experimental conditions, it is necessary to remind that the aromatic alcohols with electron donating substituent groups (EDG), as $-O-CH_3$ in different positions, show different photocatalytic activity and selectivity, in the presence of TiO_2 [30], but also by using C_3N_4 based photocatalysts [31,32]. Indeed, it is already known that the conversion of aromatic alcohols depends on the type and position of the substituent in the aromatic ring. In particular, the methoxy group in para position of the benzyl alcohol, increased both conversion and selectivity to the aldehyde. This because, the methoxy group, as Electron Donating Group (EDG), is an ortho-para orienting group, and its presence in the para position induces the attack by oxidant species to the benzyl group, thus favoring the alcohol-to-aldehyde transformation. The result obtained by using TiO_2 and C_3N_4 as photocatalysts under UV was also observed during the present investigation in the presence of CeO_2 and Au/CeO_2 photocatalysts both under UV and visible irradiation. The adsorption of 4-MBA by means of the alcoholic group on the surface of the photocatalyst and the inductive and delocalization effects caused by the $-OCH_3$ group on the aromatic ring, hinder the strong oxidizing attacks that can cause the mineralization of the molecule [31].

The photocatalytic alcohol degradation rate obtained by using all the samples are reported in Table 4. The results are in agreement with the conversion data reported in Table 3.

Table 4. Photoactivity results in terms of degradation rate of benzyl alcohol (r_{BA}) and 4-methoxybenzyl alcohol ($r_{4\text{-}MBA}$) expressed in [mM·min^{-1}], both under UV or visible light irradiation.

	UV	Vis	UV	Vis
Photocatalyst	$r_{BA} \times 10^5$	$r_{BA} \times 10^5$	$r_{4\text{-}MBA} \times 10^5$	$r_{4\text{-}MBA} \times 10^5$
CeO$_2$ A	-	-	23	15
1%Au/CeO$_2$ A	8	11	37	42
3%Au/CeO$_2$ A	11	20	69	84
CeO$_2$ hp	-	-	9	-
1%Au/CeO$_2$ hp	8	9	12	15
3%Au/CeO$_2$ hp	8	11	26	28

Bare CeO$_2$ does not produce any oxidation of BA, whereas 4-MBA was partially oxidized, faster in the presence of CeO$_2$ A than with CeO$_2$ hp. Notably, despite the band gap values of the CeO$_2$ samples, ca. 2.9 and 3.0 eV (see Figure 7) for the home prepared and Aldrich, respectively, the presence of the Au allowed the reaction to proceed with higher rates under visible irradiation than under UV one. This result is attributed to the surface plasmon resonance effect. The faster reaction was observed in the presence of 3%Au/CeO$_2$ A.

The reaction proceeds under both UV and visible light irradiation, by the two distinct mechanisms already discussed above. For that reason, the best photocatalysts (i.e., those containing 3% of Au) were tested for the 4-MBA partial oxidation also under natural solar irradiation supplying contemporaneously both UV and visible light.

2.3. Photocatalytic Activity under Natural Solar Light Irradiation

The evolution of 4-MBA concentration along with that of 4-MBAL and 4-methoxy benzoic acid (4-MBAcid) during photocatalytic experiments carried out under solar irradiation in the presence of the two 3% Au-loaded CeO$_2$ samples are reported in Figure 8. Both experiments were carried out contemporaneously, so the two reactors used received the same number of photons. During the first 30 min of the experiments, conducted in dark conditions, both catalysts adsorbed ca. 20% of the initial 4-MBA. This adsorption was slightly more evident (ca. 24%) in the case of 3%Au/CeO$_2$ A. In Figure 8 it is observed that, for both materials, during the first 30 min of irradiation the amount of aldehyde formed was greater than the amount of alcohol disappeared. This fact indicates that during the first steps of the reaction the amount of adsorbed alcohol reacting to give the aldehyde is not completely replaced by the alcohol present in the bulk of the suspension. This suggests that the amount of alcohol consistently adsorbed on the catalyst surface under irradiation is lower than that adsorbed in dark conditions. Furthermore, it cannot be excluded that part of the aldehyde formed remained adsorbed on the catalyst surface to be furtherly oxidized to 4-methoxybenzoic acid.

From the results reported in Figure 8, it was possible to calculate the conversion of 4-MBA and the selectivity versus the formation of 4-MBAL and 4-MBAcid during the evolution of the reaction. These results are reported in Figure 9.

As reported in Figure 9 for both 3% Au-loaded CeO$_2$ samples, the selectivity towards 4-MBAL was always in the range 95–98% (the highest values were observed for 3%Au/CeO$_2$ A) and it seems independent to the percentage of 4-MBA converted. The selectivity towards the formation of 4-methoxybenzoic acid was close to 5–2% (the highest values were observed for 3%Au/CeO$_2$ hp), indicating that no other species were formed during the 4-MBA partial oxidation.

In order to compare the tests carried out under natural sunlight irradiation with those conducted under UV or Vis light, the evolution of 4-MBA, 4-MBAL and 4-MBAcid concentration were also reported versus the cumulative energy entering in the reacting system per unit of volume of suspension. The results obtained under solar light irradiation are reported in Figure 10.
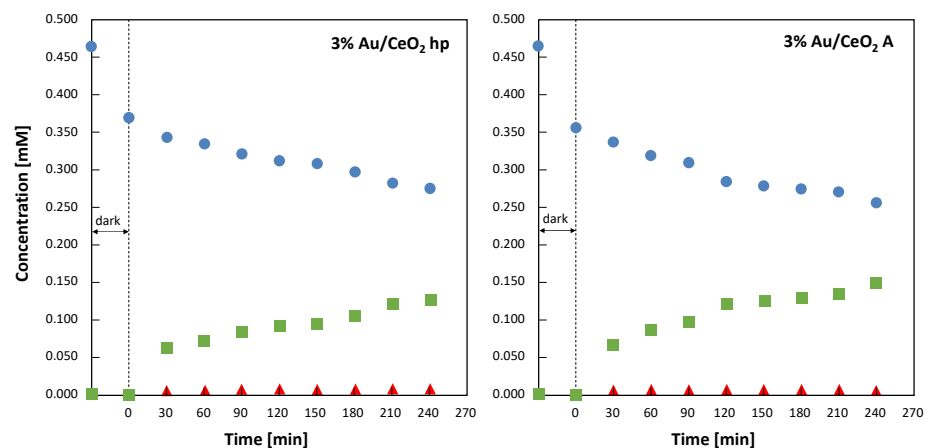
Figure 8. Natural solar light assisted partial photocatalytic oxidation of 4-MBA in the presence of the 3% Au-loaded CeO$_2$ samples. Evolution of 4-methoxybenzyl alcohol concentration (●), 4-methoxybenzaldehyde (■) and 4-methoxybenzoic acid (▲) versus natural sunlight irradiation time.
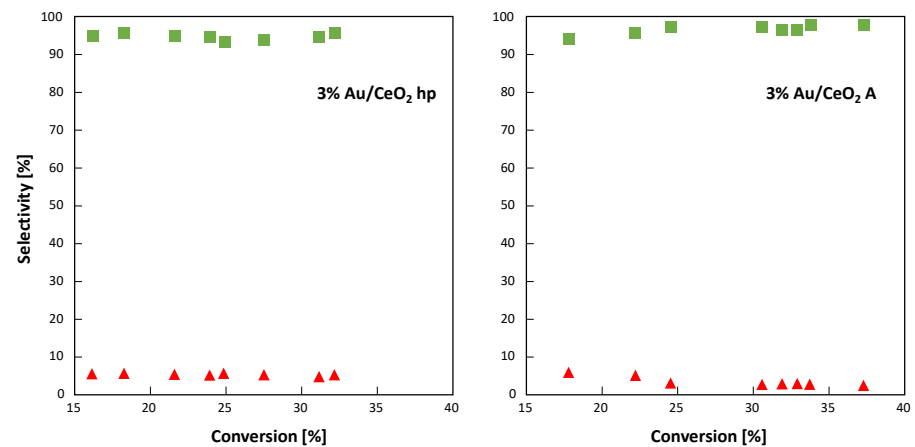
Figure 9. Natural solar light assisted partial photocatalytic oxidation of 4-MBA in the presence of the 3% Au-loaded CeO$_2$ samples. Selectivity towards 4-methoxybenzaldehyde (■) and 4-methoxybenzoic acid (▲) versus 4-methoxybenzyl alcohol conversion.
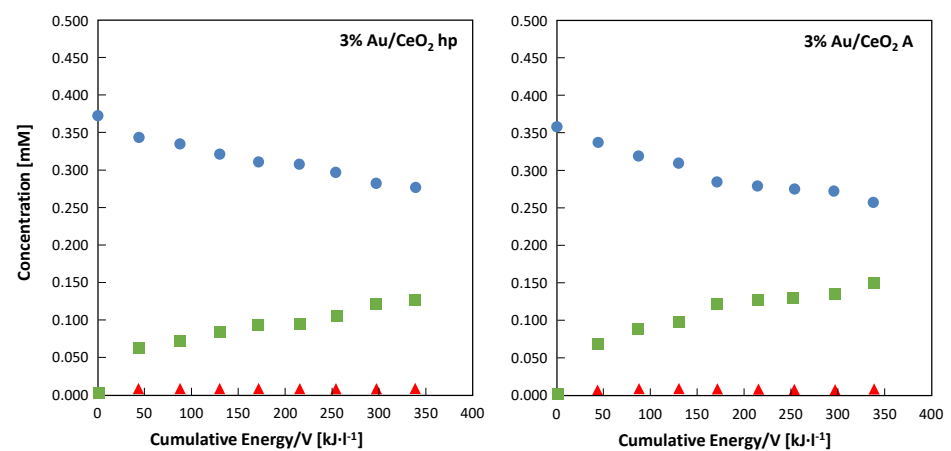
Figure 10. Natural solar light assisted partial photocatalytic oxidation of 4-MBA in the presence of the 3% Au-loaded CeO$_2$ samples. Evolution of 4-MBA concentration (●), 4-MBAL (■) and 4-MBAcid (▲) versus natural sunlight cumulative energy (in the wavelength range 315–560 nm) entering the reactor per unit of volume of suspension.

Figures 8 and 10 are representative of the same runs, consequently after 4 h of irradiation (240 min) the cumulative energy entering the reactor per unit of volume of suspension was ca. 340 $kJ \cdot L^{-1}$. It is important to consider that ca. 6% of the measured solar irradiation (20 $kJ \cdot L^{-1}$) was in the UV (315–400 nm) and the remaining part (320 $kJ \cdot L^{-1}$) in the visible range (450–560 nm). As far as the runs carried out under UV irradiation are concerned, the cumulative energy entering the reactor per unit of volume of suspension after 4 h was ca. 5 $kJ \cdot L^{-1}$, then it was much lower if compared with the amount entering under solar light irradiation. On the contrary, in the case of the tests conducted under visible light irradiation, the cumulative energy entering the reactor per unit of volume of suspension after 4 h was ca. 540 $kJ \cdot L^{-1}$ (i.e., ca. 220 $kJ \cdot L^{-1}$) more with respect to that entering during the solar tests. In Table 5 are reported the results obtained in the presence of the two photocatalysts loaded with 3% of gold after the runs carried out by irradiating the photoreactor with UV, visible or natural solar light.

Table 5. Conversion percentage of 4-MBA and selectivity percentage towards 4-MBAL after 4 h of UV, visible or natural solar irradiation for runs carried out in the presence of 3%Au/CeO$_2$ A and 3%Au/CeO$_2$ hp as photocatalysts.

Irradiation Source	Cumulative Energy per Unit of Volume [$kJ \cdot L^{-1}$]	Photocatalyst	Conversion of 4-MBA [%]	Selectivity to 4-MBAL [%]
UV light	5 [a]	3%Au/CeO$_2$ A	35	78
		3%Au/CeO$_2$ hp	13	75
Visible light	540 [b]	3%Au/CeO$_2$ A	44	95
		3%Au/CeO$_2$ hp	15	100
Natural solar light	20 [a]	3%Au/CeO$_2$ A	37	98
	320 [b]	3%Au/CeO$_2$ hp	32	96

[a] Value measured in the range 315–400 nm; [b] value measured in the range 450–560 nm.

From a perusal of Table 5 it can be concluded that the 3%Au/CeO$_2$ A photocatalyst was always the most active in terms of alcohol conversion. In particular, under both UV and visible irradiation the activity of the 3%Au/CeO$_2$ A sample was substantially higher than that obtained with the 3%Au/CeO$_2$ hp photocatalyst. On the contrary, when the reaction was carried out under natural solar light the activity of the two catalysts was similar even if the sample based on CeO$_2$ A showed to be always the most active. On the basis of the irradiation source reaching the system in the three cases, it is possible to observe that the two photocatalysts are active both under UV and visible light but the 3%Au/CeO$_2$ A sample is able to better exploit both UV and visible light irradiation when used separately. On the other hand, the 3%Au/CeO$_2$ hp photocatalyst is not very active when irradiated with UV or visible light alone. Conversely, when the latter catalyst is irradiated with sunlight containing both UV and visible, a considerable increase of activity occurs. This synergistic effect was not observed in the case of the other catalyst and consequently the activity of the two samples appeared similar.

To explain the different behavior of the two catalysts under the various types of irradiation, it is necessary to consider various factors. In particular, the porosity and the presence of metallic gold on the surface of the materials seem to be the most important ones, while the specific surface area does not seem to play an important role.

Let us now understand what happens when the catalysts are irradiated with the different sources of radiation. From the results shown in Table 5 it can be seen that the 3% Au/CeO$_2$ hp catalyst is less active under UV irradiation than the other one. This fact can be justified by considering that the 3% Au/CeO$_2$ hp material possess a greater amount of mesopores with respect the 3% Au/CeO$_2$ A sample. Mesopores that results also smaller in comparison with those showed by the latter catalyst. Consequently, the 4-MBAL formed during the early stages of irradiation could in part be retained in the pores to be further oxidized to 4-MBAcid which blocking [29] the catalytic sites strongly reduce the activity

of the catalyst. This effect is observed, although to a lower extent, also in the case of the 3% Au/CeO$_2$ A catalyst; in fact, even in this case the selectivity towards 4-MBAL does not reach 100%, indicating the formation of 4-MBAcid which remains adsorbed on the catalyst. Interestingly, under UV irradiation no 4-MBAcid was observed in solution.

Under visible irradiation, the plasmonic effect, causing strong local heating, favors the 4-MBAL desorption, avoiding its subsequent oxidation to 4-MBAcid. This fact is evidenced by the high selectivity towards 4-MBAL (ca. 100%) observed under visible light irradiation with both catalysts. The fact that the 3% Au/CeO$_2$ hp catalyst was still not very active also under visible irradiation can be justified considering that the gold deposited in this catalyst is essentially in ionic form (see XPS study) and consequently the plasmonic effect responsible for the photoactivity was less marked.

Furthermore, the lower gold-support interaction in the case of the 3% Au/CeO$_2$ hp catalyst, as evidenced by diffuse reflectance investigation, can contribute to the low activity of this material. Under natural solar light irradiation it was observed that the activity of the 3% Au/CeO$_2$ hp catalyst increased. This fact can be related to the UV energy density entering the system that was 20 kJ·L^{-1} (i.e., four times higher than that measured during the test carried out under UV lamp irradiation (5 kJ·L^{-1})). Consequently, it is possible to assume that the 3% Au/CeO$_2$ hp catalyst is essentially activated by UV; indeed, under solar irradiation the amount of visible light reaching the reactor (320 kJ·L^{-1}) was lower with respect to the test conducted by irradiating the system by using visible LED (540 kJ·L^{-1}). However, the presence of visible light was still beneficial because the plasmonic effect help the reaction by favoring the desorption of the 4-MBAL; indeed, for these runs the selectivity towards the formation of aldehyde was always close to 100% (see Table 5). Resuming for the 3% Au/CeO$_2$ hp catalyst, the enhanced photocatalytic activities can be attributed to the synergistic effect between the Au nanocrystal acting as the plasmonic component for efficiently harvesting the light and the CeO$_2$ support providing catalytically active sites for the oxidation reaction. On the other hand, in the case of the 3% Au/CeO$_2$ A catalyst, which was almost active even under irradiation with visible light, the additional UV contribution of solar radiation did not significantly increase the activity of the catalyst.

It is interesting to compare the conversion, selectivity and reaction rate obtained with the photocatalysts in this study with respect to those reported in literature for the same reaction.

Li et al. study the partial oxidation of benzyl alcohol with a 100% selectivity to benzaldehyde in the presence of 0.25–0.5 wt.% Au/CeO$_2$ samples using acetonitrile as the solvent and the irradiation of λ > 420 nm [15]. They reported a maximum conversion rate of ca. 2250 and ca. 390 μmol·h^{-1}·g^{-1} under UV–Vis or only visible irradiation, respectively. These results are better than those obtained in our work (ca. 36 μmol·h^{-1}·g^{-1} under visible light) but they are not comparable because we have used water as solvent. Moreover, the UV and visible photon flux emitted by the Xe lamp used by Li et al. were much higher with respect to our light source. Kominami et al. studied the photocatalytic oxidation of benzyl alcohol in aqueous suspensions of Au/CeO$_2$ samples under irradiation by green light from an LED. They prepared Au/CeO$_2$ nanocomposites by two photodeposition methods, both exhibiting LSPR absorption at around 550 nm matching with the wavelength of the green LED light used in their research [16]. They conclude that the size of the nanoparticles affected the intensity of the photoabsorption and hence the photocatalytic activity as previously observed in plasmonic Au/TiO$_2$/photocatalysts [33]. The authors have shown that the benzyl alcohol was completely consumed after 15 to 20 h depending upon de material and experimental conditions. Benzaldehyde was formed from benzyl alcohol partial photo-oxidation with a >99% selectivity. The rates of benzaldehyde formation were determined to be in the range 1.9 to 3.0 μmol h^{-1}. These results were very close to those obtained in this work using the visible LED (in Table 4, 20·10^{-5} mM min^{-1} correspond to 1.8 μmol h^{-1}). Cui et al. studied the selective photocatalytic conversion of alcohols (benzyl alcohol, 4-methoxybenzyl alcohol) using Au/CeO$_2$ composites with different Au loadings under visible light irradiation (λ > 400 nm, light intensity of 0.7 W cm^{-2} by

using benzotrifluoride as solvent [34]. The conversion achieved a 100% in the presence of Au 4 wt.%/CeO$_2$ after 4 h of reaction and the selectivity to benzaldehyde was ca. 95%. Wolski et al. prepared three CeO$_2$ samples using different co-precipitation agents (urea, hexamethylenetetramine or NaOH) and Au-loaded photocatalysts. The catalytic study was carried out in dark condition at 40 °C (thermal catalysis) and evidenced that the most active catalysts (highest conversion of benzyl alcohol) were those containing gold and in particular the one prepared by using NaOH as co-precipitation agent [19]. The results obtained by Wolski et al. are not comparable with those reported in this work but indicate that, in order to avoid the over oxidation of benzyl alcohol to benzoic acid, it is better to carry out the experiments at room temperature, as in our case. By using the best catalyst they obtained benzoic acid. With a conversion after 40 min of 47% with a selectivity to benzoic acid of 91%, the benzaldehyde was obtained with a 9% of selectivity. Furthermore, in our opinion, the use of a basic solution for the experiments could significantly influence the results.

3. Materials and Methods

3.1. Preparation of Au/CeO$_2$ Photocatalysts

All the used reagents (Sigma-Aldrich) were of analytical grade with purity $\geq$99.5%. The home-prepared (hp) cerium oxide was synthesized via hydrothermal method. In details, for a typical preparation, 6 g of Ce(NO$_3$)$_3$·6H$_2$O were dissolved in 30 mL of H$_2$O then, 40 mL of NaOH solution (2.5 mol·L^{-1}) were added under vigorous stirring. The resulting slurry was rapidly transferred into a 100 mL Teflon autoclave and heated in oven at 120 °C for 23 h. The aged precipitate was collected by filtration, washed with abundant deionized water until neutrality and finally with ethanol. The powder was dried overnight at 60 °C and calcined at 350 °C for 3 h (heating rate 2 °C·min^{-1}). This sample was denoted CeO$_2$ hp. For comparison purpose, a commercial cerium oxide was purchased from Sigma-Aldrich and herein is labelled as CeO$_2$ A.

Supported gold catalysts were prepared by deposition-precipitation method. The support (CeO$_2$ A or CeO$_2$ hp) was preliminary suspended in water, then, gold was deposited by adding a solution of HAuCl$_4$·3H$_2$O (0.01 mol·L^{-1}) corresponding to 1 or 3 wt.% of Au in the catalyst. After stirring at room temperature for 1 h in order to favor a preliminary interaction between the Au precursor and the hydroxyl groups of the support, the pH of the solution was set to ~7.5–8.0 by adding K$_2$CO$_3$ (0.05 mol·L^{-1}) and the temperature was increased to 65 °C. The suspension was stirred overnight at this temperature. After filtering and careful washing with hot deionized water, the catalyst was dried overnight at 100 °C, and then calcined at 350 °C for 2 h (heating rate 2 °C·min^{-1}). The resulting catalysts were labelled as 1% and 3%Au/CeO$_2$ A or 1% and 3%Au/CeO$_2$ hp.

3.2. Characterization of the Materials

The crystalline structure of the samples was determined by powder X-ray diffraction patterns (XRD), performed on a Bruker D5000 diffractometer equipped with a Kristalloflex 760 X-ray generator (Bruker AXS GmbH, Karlsruhe, Germany) and with a curved graphite monochromator using Cu Kα radiation (40 kV/30 mA). The data were recorded in a 2θ range of 20°–80° with a step size of 0.05° and time per step of 20 s. The crystalline phases of samples were analyzed according to ICSD (Inorganic Crystal Structure Database) files. The mean crystallite size was calculated by the Debye–Scherrer equation: D = 0.9λ/Bcosθ, where D represents the average crystalline size, 0.9 is the Scherrer parameter, λ is the wavelength of the X-ray radiation (0.15406 nm), B denotes the full width at half maximum of the peak (FWHM), and θ is the angular position of the main peak, the (111) for CeO$_2$ and Au phases, as well.

The Specific surface area (SSA), pore volume and mean pore diameter of the materials were measured by N$_2$ adsorption−desorption isotherms using a Micromeritics ASAP 2020 apparatus. Before analysis, the samples were degassed in vacuum at 250 °C for 2 h, and then the measurements were performed at liquid nitrogen temperature

(-196 °C). The Brunauer$-$Emmett$-$Teller (BET) method was used to calculate the SSA. The Barrett$-$Joyner$-$Halenda (BJH) method was applied to the desorption branch to estimate the mesoporous pore volume and the average pore diameter (in the range 2–50 nm). The total pore volume was measured as single desorption point, at p/p_0 = 0.95. The micropores volume was calculated by t-Plot.

Scanning electron microscopy (SEM) was performed by using a FEI Quanta 200 ESEM microscope, operating at 20 kV on specimens upon which a thin layer of gold had been evaporated. On the other hand, an electron microprobe used in an energy dispersive mode (EDX) was employed to obtain information on the actual Au and Ce content present in the samples.

TEM (transmission electron microscopy) analysis was performed with an S/TEM ThermoFisher Talos F200S operating at 200 kV. The microscope is equipped with an integrated EDS (Energy Dispersive X-rays Spectroscopy) system with two windowless silicon drift detectors (SDD). The samples were observed in both TEM and STEM mode by using bright field (BF) and high-angle annular dark-field (HAADF) detectors. Moreover, the STEM mode allows evaluating the actual elemental distribution in the sample collecting EDS maps. Samples were dispersed in ethanol and a 50 μL drop of the dispersion were deposited on TEM copper support grids covered by an amorphous carbon film. The X-ray photoelectron spectroscopy (XPS) analyses of the samples were performed with a VG Microtech ESCA 3000 Multilab (VG Scientific, Sussex, UK), using Al Kα source (1486.6 eV) run at 14 kV and 15 mA, and CAE analyzer mode. For the individual peak energy regions, a pass energy of 20 eV set across the hemispheres was used. The constant charging of the samples was removed by referencing all the energies to the C 1s peak energy set at 285.1 eV, arising from adventitious carbon. Analyses of the peaks were performed using the CASA XPS software (version 2.3.17, Casa Software Ltd. Wilmslow, Cheshire, UK, 2009). For the peak shape a Gaussian (70%)-Lorentzian (30%) line shape, defined in Casa XPS as GL(30) profiles were used for each component of the main peaks after a Shirley type baseline subtraction. The binding energy values were quoted with a precision of $\pm$0.15 eV, and the atomic percentage with a precision of $\pm$10%.

UV–visible diffused reflectance spectra (DRS) of the samples were obtained for the dry-pressed film samples using a UV–visible spectrophotometer (UV-2550, Shimadzu, Japan). $BaSO_4$ was used as a reflectance standard in a UV–visible diffuse reflectance experiment.

3.3. Photocatalytic Activity Tests

The photocatalytic experiments were carried out by using three different set-ups. In the first one, a Pyrex cylindrical photoreactor (internal diameter: 32 mm, height: 188 mm) containing 150 mL of aqueous suspension was used. The photoreactor was irradiated externally by three Actinic BL TL MINI 15 W/10 Philips fluorescent lamps located at 3 cm distance from the reactor axis. The lamps emitted in the 340–420 wavelength range with the main emission peak at 365 nm. The impinging radiation energy in the range 315–400 nm was measured by a radiometer Delta Ohm DO9721 with an UVA probe and its average value was 2.7 W m^{-2}. In the second set-up, a Pyrex batch photoreactor of cylindrical shape containing 150 mL of aqueous suspension was used. 120 W visible LED was positioned externally in a co-axial position surrounding the photoreactor. The average radiation energy impinging the reactor was ca. 300 W$\cdot$m^{-2} in the 450–560 nm range. The emission in 315–400 nm range was null. In both the set-ups all the photons emitted by the lamps completely reached the suspension.

During the experiments, both reactors were open, and the equilibrium between dissolved O_2 in the aqueous suspension and in the atmosphere was achieved. The reaction was carried out at ca. 25 °C as the reactors were provided by a thimble where water was allowed to circulate. Benzyl alcohol (BA) and 4-hydroxy benzyl alcohol (4-MBA) were used as the substrates, and their initial concentration in water was 0.5 mM at natural pH.

Before starting the irradiation, 50 mg of catalyst (0.33 g L^{-1}) were added to the solution and the obtained suspension was kept in an ultrasonic bath for 10 min and stirred

under dark for 30 min, to attain the adsorption equilibrium. Throughout the reaction, samples of the irradiated suspension were withdrawn every 30 min and filtered through 0.25 μm membranes (HA, Millipore) to separate the photocatalyst particles before the HPLC analyses. All the aromatic molecules (i.e., BA and 4-MBA) but also the corresponding aldehydes (i.e., benzaldehyde (BAL) and 4-methoxybenzaldehyde (4-MBAL)), along with the corresponding carboxylic acids, were analyzed by a Beckman coulter HPLC apparatus equipped with a Diode Array detector and a Phenomenex KINETEK 5 μm C18 instead. The eluent (0.8 mL min^{-1}) consisted of a mixture of acetonitrile and 13 mM trifluoroacetic acid (20:80 *v:v*). Standards purchased from Sigma-Aldrich with a purity >99% were used to identify the products and to obtain the calibration curves.

Further experiments, by using the natural solar light irradiation, were carried out on clear sunny days in Palermo (Italy) from 9:30 to 13:30. Typically, 75 mL of 0.5 mM 4MBA solution and 25 mg of photocatalyst were introduced inside a round-shaped Pyrex batch reactor having a total volume of 125 mL and a diameter of 10 cm. The reactor was closed and no gases were fed during the tests as preliminary experiments indicated that O_2 deriving from air and present in the system was enough to induce the oxidation reaction. The suspension was continuously magnetically stirred and approximately 2.5 mL were withdrawn every 30 min and analyzed by using the previously described analytical procedure. In order to assess the cumulative photon energy entering in the photoreactor, the photon flux reaching the reacting suspension in the range 315–560 nm was measured every 10 min throughout the photocatalytic tests by using the same radiometer above described.

4. Conclusions

In this work, two type of CeO_2 (i.e., a commercial one and a home prepared one) were used as support of Au nanoparticles at two different percentages of metal (1 and 3 wt. %). All materials were investigated as photocatalysts for the photocatalytic selective oxidation of benzyl alcohol and 4-methoxybenzyl alcohol to the correspondent benzaldehydes, in aqueous suspensions and room conditions under UV, visible and natural solar light irradiation. Bare CeO_2 samples resulted active under UV light and virtually inactive under visible light irradiation. The presence of Au improved both the conversion of the alcohols and the selectivity of the reaction towards the aldehyde, showing good activity, particularly under visible and natural solar light irradiation. This fact was attributed to the presence of the Au nanoparticles that caused a strong visible radiation absorption at 565–570 nm associated to the localized surface plasmon resonance (LSPR) of this metal. Moreover, the photo-induced activity of the materials increased by increasing the Au content.

The activity of Au/CeO_2 plasmonic photocatalysts prepared in this work was similar to those reported in previous studies, but here it was shown the possibility to successfully carry out the partial oxidation of benzyl alcohols in water solution under natural sunlight, reaching high conversion after only 4 h of irradiation (ca. 37% in the case of 3%Au/CeO_2 A sample), and in particular high selectivity versus the aldehyde production (ca. 98%). This fact was explained by considering the ability of these materials to exploiting the synergistic effect between the Au nanoparticles acting as plasmonic component for efficiently harvesting the visible light and the CeO_2, that provides photo-active sites for the oxidation reaction under UV light irradiation.

References

1. García-López, E.I.; Palmisano, L. (Eds.) *Materials Science in Photocatalysis*, 1st ed.; Elsevier: Amsterdam, The Netherlands, 2021.
2. García, M.A. Surface plasmons in metallic nanoparticles: Fundamentals and applications. *J. Phys. D Appl. Phys.* **2011**, *44*, 283001–283020. [CrossRef]
3. Li, S.; Cai, J.; Wu, X.; Liu, B.; Chen, Q.; Li, Y.; Zheng, F. TiO_2@Pt@CeO_2 nanocomposite as a bifunctional catalyst for enhancing photo-reduction of Cr (VI) and photo-oxidation of benzyl alcohol. *J. Hazard. Mater.* **2018**, *346*, 52–61. [CrossRef]
4. Chen, X.; Zhu, H.Y.; Zhao, J.C.; Zheng, Z.T.; Gao, X.P. Visible-light-driven oxidation of organic contaminants in air with gold nanoparticle catalysts on oxide supports. *Angew. Chem. Int. Ed.* **2008**, *47*, 5353–5356. [CrossRef]
5. Kraeutler, B.; Bard, A.J. Heterogeneous photocatalytic preparation of supported catalysts. Photodeposition of platinum on TiO_2 powder and other substrates. *J. Am. Chem. Soc.* **1978**, *100*, 4317–4318. [CrossRef]
6. Mock, J.J.; Barbic, M.; Smith, D.R.; Schultz, D.A.; Schultz, S. Shape effects in plasmon resonance of individual colloidal silver nanoparticles. *J. Chem. Phys.* **2002**, *116*, 6755–6759. [CrossRef]
7. Cheng, H.; Fuku, K.; Kuwahara, Y.; Mori, K.; Yashita, H. Harnessing single-active plasmonic nanostructures for enhanced photocatalysis under visible light. *J. Mater. Chem. A* **2015**, *3*, 5244–5258. [CrossRef]
8. Chen, H.; Shao, L.; Li, Q.; Wang, J. Gold nanorods and their plasmonic properties. *Chem. Soc. Rev.* **2013**, *42*, 2679–2724. [CrossRef]
9. Zhao, G.; Zozuka, H.; Yoko, T. Sol-gel preparation and photoelectrochemical properties of TiO_2 films containing Au and Ag metal particles. *Thin Solid Films* **1996**, *277*, 147–154. [CrossRef]
10. Li, B.; Gu, T.; Ming, T.; Wang, J.; Wang, P.; Wang, J.; Yu, J.C. Gold Core@(Ceria Shell) nanostructures for plasmon-enhanced catalytic reactions under visible light. *ACS Nano* **2014**, *8*, 8152–8162. [CrossRef]
11. Kuo, C.H.; Yang, Y.C.; Gwo, S.; Huang, M.H. Facet-dependent and au nanocrystal-enhanced electrical and photocatalytic properties of Au−Cu_2O core-shell heterostructures. *J. Am. Chem. Soc.* **2011**, *133*, 1052–1057. [CrossRef]
12. Kong, L.; Chen, W.; Ma, D.K.; Yang, Y.; Liu, S.S.; Huang, S.M. Size control of Au@ Cu_2O octahedra for excellent photocatalytic performance. *J. Mater. Chem.* **2012**, *22*, 719–724. [CrossRef]
13. Lu, B.; Quan, F.; Sun, F.; Jia, F.; Zhang, L. Photothermal reverse-water-gas-shift over Au/CeO_2, with high yield and selectivity in CO_2 conversion. *Catal. Commun.* **2019**, *129*, 105724. [CrossRef]
14. Brink, J.; Arends, I.W.C.E.; Sheldon, R.A. Green, catalytic oxidation of alcohols in water. *Science* **2000**, *287*, 1636–1639. [CrossRef] [PubMed]
15. Li, B.; Zhang, B.; Nie, S.; Shao, L.; Hu, L. Optimization of plasmon-induced photocatalysis in electrospun Au/CeO_2 hybrid nanofibers for selective oxidation of benzyl alcohol. *J. Catal.* **2017**, *348*, 256–264. [CrossRef]
16. Tanaka, A.; Hashimoto, K.; Kominami, H. Preparation of Au/CeO_2 exhibiting strong surface plasmon resonance effective for selective or chemoselective oxidation of alcohols to aldehydes or ketones in aqueous suspensions under irradiation by green light. *J. Am. Chem. Soc.* **2012**, *134*, 14526. [CrossRef] [PubMed]
17. Ishida, T.; Murayama, T.; Taketoshi, A.; Haruta, M. Importance of size and contact structure of gold nanoparticles for the genesis of unique catalytic processes. *Chem. Rev.* **2020**, *120*, 464–525. [CrossRef]
18. Engel, J.; Schwartz, E.; Catlow, C.R.A.; Roldan, A. The influence of oxygen vacancy and Ce^{3+} ion positions on the properties of small gold clusters supported on $CeO_{2−x}$(111). *J. Mater. Chem. A* **2020**, *8*, 15695–15705. [CrossRef]
19. Wolski, L.; Nowaczyk, G.; Jurga, S.; Ziolek, M. Influence of co-precipitation agent on the structure, texture and catalytic activity of Au-CeO_2 catalysts in low-temperature oxidation of benzyl alcohol. *Catalysts* **2021**, *11*, 641. [CrossRef]
20. Burroughs, P.; Hamnett, A.; Orchard, A.F.; Thornton, G. Satellite structure in the X-ray photoelectron spectra of some binary and mixed oxides of lanthanum and cerium. *J. Chem. Soc. Dalt. Trans.* **1976**, 1686–1698. [CrossRef]
21. Henderson, M.A.; Perkins, C.L.; Engelhard, M.H.; Thevuthasan, S.; Peden, C.H.F. Redox properties of water on the oxidized and reduced surfaces of CeO_2(111). *Surf. Sci.* **2003**, *526*, 1–18. [CrossRef]
22. Pardo, A.; Feliú, S.; Merino, M.C.; Arrabal, R.; Matykina, E. The effect of cerium and lanthanum surface treatments on early stages of oxidation of A361 aluminium alloy at high temperature. *Appl. Surf. Sci.* **2007**, *254*, 586–595. [CrossRef]
23. Károlyi, J.; Németh, M.; Evangelisti, C.; Sáfrán, G.; Schay, Z.; Horváth, A.; Somodi, F. Carbon dioxide reforming of methane over Ni–In/SiO_2 catalyst without coke formation. *J. Ind. Eng. Chem.* **2018**, *58*, 189–201. [CrossRef]
24. Casaletto, M.P.; Longo, A.; Martorana, A.; Prestianni, A.; Venezia, A.M. XPS study of supported gold catalysts: The role of Au0 and Au+δ species as active sites. *Surf. Interf. Anal.* **2006**, *38*, 215–218. [CrossRef]
25. Ke, X.; Zhang, X.; Zhao, J.; Sarina, S.; Barry, J.; Zhu, H. Selective reductions using visible light photocatalysts of supported gold nanoparticles. *Green Chem.* **2013**, *15*, 236–244. [CrossRef]
26. Tauc, J. Absorption edge and internal electric fields in amorphous semiconductors. *Mater. Res. Bull.* **1970**, *5*, 37–46. [CrossRef]
27. Sarina, S.; Waclawick, E.R.; Zhu, H. Photocatalysis on supported gold and silver nanoparticles under ultraviolet and visible light irradiation. *Green Chem.* **2013**, *15*, 1814–1833. [CrossRef]
28. Wang, P.; Baibiao, H.; Dai, Y.; Whangbo, M.H. Plasmonic photocatalysts: Harvesting visible light with noble metal nanoparticles. *Phys. Chem. Chem. Phys.* **2012**, *14*, 9813–9825. [CrossRef] [PubMed]
29. Marcì, G.; Addamo, M.; Augugliaro, V.; Coluccia, S.; García-López, E.; Loddo, V.; Martra, G.; Palmisano, L.; Schiavello, M. Photocatalytic oxidation of toluene on irradiated TiO_2: Comparison of degradation performance in humidified air, in water and in water containing a zwitterionic surfactant. *J. Photochem. Photobiol. A Chem.* **2003**, *160*, 105–114. [CrossRef]

30. Palmisano, G.; Addamo, M.; Augugliaro, V.; Caronna, T.; Di Paola, A.; García-López, E.I.; Loddo, V.; Marcì, G.; Palmisano, L.; Schiavello, M. Selectivity of hydroxyl radical in the partial oxidation of aromatic compounds in heterogeneous photocatalysis. *Catal. Today* **2007**, *122*, 118–127. [CrossRef]

31. García-López, E.I.; Abbasi, Z.; Di Franco, F.; Santamaria, M.; Marcì, G.; Palmisano, L. Selective oxidation of aromatic alcohols in the presence of C_3N_4 photocatalysts derived from the polycondensation of melamine, cyanuric and barbituric acids. *Res. Chem. Interm.* **2021**, *47*, 131–156. [CrossRef]

32. Krivtsov, I.; Ilkaeva, M.; García-López, E.I.; Marcì, G.; Palmisano, L.; Bartashevich, E.; Grigoreva, E.; Matveeva, K.; Díaz, E.; Ordóñez, S. Effect of substituents on partial photocatalytic oxidation of aromatic alcohols assisted by polymeric C_3N_4. *ChemCatChem* **2019**, *11*, 2713–2724. [CrossRef]

33. Tanaka, A.; Hashimoto, K.; Kominami, H. A very simple method for the preparation of Au/TiO_2 plasmonic photocatalysts working under irradiation of visible light in the range of 600–700 nm. *Chem. Commun.* **2017**, *53*, 4759–4762. [CrossRef]

34. Cui, Z.; Wang, W.; Zhao, C.; Chen, C.; Han, M.; Wang, G.; Zhang, Y.; Zhang, H.; Zhao, H. Spontaneous redox approach to the self-assembly synthesis of Au/CeO_2 plasmonic photocatalysts with rich oxygen vacancies for selective photocatalytic conversion of alcohols. *ACS Appl. Mater. Interfaces* **2018**, *10*, 31394–31403. [CrossRef]